View metadata, citation and similar papers at core.ac.uk

brought to you by CORE

provided by Archivio istituzionale della ricerca - Politecnico di Milano

Journal of
Applied
Crystallography

ISSN 1600-5767

Received 10 August 2014
Accepted 28 October 2014

Reconstruction of crystal shapes by X-ray nanodiffraction from three-dimensional superlattices

Mojmír Meduňa,[a,b]* Claudiu V. Falub,[c]‡ Fabio Isa,[d]¶ Daniel Chrastina,[d] Thomas Kreiliger,[c] Giovanni Isella[d] and Hans von Känel[c]

[a]Department of Condensed Matter Physics, Masaryk University, Kotlářská 2, Brno 61137, Czech Republic, [b]CEITEC, Masaryk University, Kamenice 5, Brno 60177, Czech Republic, [c]Laboratory for Solid State Physics, ETH Zurich, Otto-Stern-Weg 1, Zurich 8093, Switzerland, and [d]L-NESS, Department of Physics, Politecnico di Milano, Via Anzani 42, Como 22100, Italy. Correspondence e-mail: mjme@physics.muni.cz

Quantitative nondestructive imaging of structural properties of semiconductor layer stacks at the nanoscale is essential for tailoring the device characteristics of many low-dimensional quantum structures, such as ultrafast transistors, solid state lasers and detectors. Here it is shown that scanning nanodiffraction of synchrotron X-ray radiation can unravel the three-dimensional structure of epitaxial crystals containing a periodic superlattice underneath their faceted surface. By mapping reciprocal space in all three dimensions, the superlattice period is determined across the various crystal facets and the very high crystalline quality of the structures is demonstrated. It is shown that the presence of the superlattice allows the reconstruction of the crystal shape without the need of any structural model.

© 2014 International Union of Crystallography

1. Introduction

Rapid advances in the past few years in the focusing of X-rays at third-generation synchrotron light sources have made it possible to tremendously increase the spatial resolution of X-ray scattering techniques (Stangl *et al.*, 2014). Scanning experiments with beam diameters of the order of a few hundred nanometres have allowed the determination of the strain and shape of individual quantum dots and wires (Hanke *et al.*, 2008; Mocuta *et al.*, 2008; Stangl *et al.*, 2009; Biermanns *et al.*, 2013), of dot molecules (Dubslaff *et al.*, 2010, 2012), of nanopatterned ridges (Chrastina *et al.*, 2012), and even of the channel region of a working field-effect transistor (Hrauda *et al.*, 2011). X-ray beams focused down to the nanometre scale have also been used for mapping the crystal quality of mosaic layers (Stefenelli *et al.*, 2013), graded films (Bartosik *et al.*, 2013), films grown on patterned substrates (Mondiali *et al.*, 2014) and organic electronic devices (Paci *et al.*, 2013). Recently the focusing of hard X-rays has been pushed down to below 5 nm (Mimura *et al.*, 2010; Krüger *et al.*, 2012; Döring *et al.*, 2013). This will offer unique opportunities in the near future for X-ray imaging of structural properties with outstanding spatial resolution.

In addition, extraordinary brilliance at synchrotron sources and beam focusing allow experiments that require high beam coherency to be performed (Pfeifer *et al.*, 2006; Robinson & Harder, 2009). Coherent diffraction experiments and phase retrieval algorithms can be used to obtain the shape of nanoparticles (Takahashi *et al.*, 2010; Chamard *et al.*, 2010), although only objects of limited size can be measured. In combination with a nanofocused X-ray beam, Bragg projection ptychography (Godard *et al.*, 2011) has provided information about lattice strain in SiGe semiconductor devices (Hruszkewycz *et al.*, 2012). Nanodiffraction experiments are also used in combination with other techniques such as atomic force microscopy (Scheler *et al.*, 2009) or micro-Raman spectroscopy (Davies *et al.*, 2009). Moreover, the development of advanced two-dimensional X-ray detectors and highly collimated synchrotron beams allows for fast three-dimensional reciprocal space mapping at high resolution (Scheler *et al.*, 2009; Cornelius *et al.*, 2011).

Here, we report on X-ray diffraction measurements carried out using both a laboratory source and a nanofocused synchrotron source on Ge-rich three-dimensional SiGe crystals epitaxically grown on deeply patterned Si substrates. The micrometre-sized crystals exhibit facetted morphology and contain strain-symmetrized SiGe/Ge superlattices (SLs) parallel to the facet planes. By illuminating various facets of an individual crystal we determine the corresponding periodicities of the SLs and demonstrate that the heteroepitaxial structure exhibits a very high crystalline quality. We show that the presence of the SLs reveals the crystal morphology in a straightforward manner without the need of a structural model.

‡ Present Address: OC Oerlikon Advanced Technologies, Iramali 18, 9496 Balzers, Liechtenstein.
¶ Present Adress: Laboratory for Solid State Physics, ETH Zurich, Otto-Stern-Weg 1, Zurich 8093, Switzerland.

2. Samples

SL-containing SiGe crystals with a nominal Ge content of 90% were grown by low-energy plasma-enhanced chemical vapor deposition (LEPECVD) (Rosenblad *et al.*, 2000) on Si substrates deeply patterned at a micrometre scale. We have previously shown for the case of pure Ge that this method can provide space filling arrays of epitaxial crystals of excellent quality despite the lattice mismatch of 4.2% between Ge and Si (Falub *et al.*, 2012). The $Si_{0.1}Ge_{0.9}$ crystals were deposited to a height of 8 µm at a substrate temperature T = 903 K and a growth rate of ∼4 nm s^{-1}. The SLs on top of the $Si_{0.1}Ge_{0.9}$ crystals consisted of 50 periods of $Si_{0.15}Ge_{0.85}$/Ge with nominal thicknesses of 21 and 10 nm derived from rate calibration on planar material for the SiGe barriers and Ge quantum wells, respectively (Pezzoli *et al.*, 2014; Falub *et al.*, 2014). The SL stack was grown at a substrate temperature of 743 K at the same rate. Fig. 1(*a*) shows a scanning electron microscopy (SEM) image of an intentionally damaged array of SL crystals grown on Si(001) patterned into 2 × 2 µm wide pillars. The latter are separated by 4 µm wide trenches oriented along the ⟨110⟩ substrate directions. The X-ray diffraction experiments with the laboratory source were carried out on intact arrays of the same kind. For the nanodiffraction experiments, however, the preparation of isolated crystals was found to be more convenient in order to avoid crosstalk due to beam penetration through neighboring crystals. Such isolated crystals were obtained by removing surrounding crystals by means of a micromanipulator inside an electron microscope (Falub *et al.*, 2013).

As follows from the growth kinetics (Bergamaschini *et al.*, 2013), the crystal surface (Fig. 1*a*) is composed mainly of {113} facets on top and {111} and {110} facets on the sides. Thus, the main focus of this paper will be on the SL structure on this top faceted surface.

3. Method

The source X-ray beam is represented by the wavevector $\mathbf{K}_0$ and the scattered radiation by the wavevector $\mathbf{K}_s$, with the scattering vector $\mathbf{Q} = \mathbf{K}_s - \mathbf{K}_0$. Since the scattering is considered to be perfectly elastic, $|\mathbf{K}_s| = |\mathbf{K}_0|$. A sketch of the scattering geometry may be seen in Fig. 1(*b*). The angular aperture of both the incident and the exit wavevectors, defining the resolution, is determined by the beam and receiving optics (Falub *et al.*, 2013; Pietsch *et al.*, 2004). The scattering intensity is then represented in reciprocal space as a function of the scattering vector coordinates $\mathbf{Q} = (Q_x, Q_y, Q_z)$, *i.e.* as a reciprocal space map (RSM). According to kinematical X-ray scattering theory, the scattered intensity for a parallel beam is proportional to the absolute square of the Fourier transform (FT) of the electron density at each individual point of the crystal (Pietsch *et al.*, 2004). The reciprocal lattice points are observed as FTs of the probed crystal shape. They are represented by truncation rods perpendicular to each irradiated planar crystal surface. The rods are combined with the diffusely scattered signal from crystal imperfections. The scattering intensity and its distribution in reciprocal space thus contain information about the deviations of the atoms from their positions in a perfect crystal. These deviations, which may be the result both of lattice tilt and strain and of random displacements caused by defects and thermal motion, are responsible for diffuse scattering. In order to extract all structural information one usually needs a complicated model, since phase information is lost unless coherent beams and very small objects are used together with complex phase retrieval techniques (Stangl *et al.*, 2014).

For the laboratory measurements we used a SmartLab Rigaku diffractometer equipped with a rotating Cu anode source operated at 45 kV and 140 mA. The beam optics comprised standard channel cut crystals, with a 2 × Ge(220) monochromator in the source beam to select Cu $K\alpha_1$ radiation and a 2 × Ge(220) analyzer crystal in front of the scintillation detector. The out-of-scattering-plane resolution along Q_y was increased by Soller slit blades arranged parallel to the scattering plane with various apertures ranging from 0.115 to 5°. The typical size of the X-ray beam at the sample surface was 1.0 × 5.0 mm. RSMs were recorded around symmetric (004) and asymmetric (224) Bragg reflections.

The X-ray nanodiffraction experiment was performed at the ID01 beamline of the European Synchrotron Radiation Facility (ESRF) in Grenoble. The beam, with energy 11.07 keV, was focused down to 300 × 500 nm using a Fresnel zone plate (FZP) (Stangl *et al.*, 2014; Hrauda *et al.*, 2011; Falub *et al.*, 2013). The small beam size allowed us to scan one selected individual SL crystal along its height and to record the scattering intensity at a set of mesh points in the *xy* plane parallel to the macroscopic sample surface. The sample was translated within the *xy* plane by means of a piezo-stage mounted on the Huber goniometer. The scattering intensity was recorded by a two-dimensional pixel detector (MAXIPIX). Three-dimensional RSMs at various (*x*, *y*) points in the surface plane were

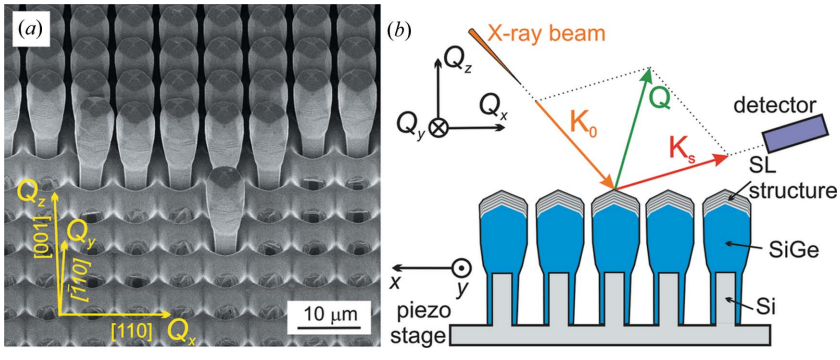

Figure 1
(*a*) Perspective-view SEM micrograph of 8 µm tall $Si_{0.1}Ge_{0.9}$ crystals with the embedded SL structure on top; for the nanodiffraction experiments one crystal was isolated from the rest. (*b*) Schematic sketch of the scattering geometry with the incident beam $\mathbf{K}_0$ and exit beam $\mathbf{K}_s$ defining the scattering vector $\mathbf{Q}$.

constructed from sequences of two-dimensional surface meshes recorded at various incidence angles. Because of goniometer limitations at the beamline, the RSMs were recorded around the 115 Bragg reflection in the nanodiffraction case.

In our description of X-ray scattering in terms of FTs given above, we have ignored the role played by the instrumental resolution of the experimental setup. As a matter of fact, the observed scattering intensity is given not by the bare FT of the irradiated crystal volume but rather by its convolution with the instrumental resolution function. For a nanofocused X-ray beam probing a micrometre-sized crystal, the situation is especially complex. In the scattering geometry of Fig. 1(*b*) the path length of the beam traversing the elongated vertical microcrystal is much smaller than the distance between the FZP and the sample. One can therefore approximate the irradiated region as a cylinder of diameter d and length h, as indicated in Fig. 2(*a*). The FT of the illuminated region can therefore be approximated by a disc of diameter $\Delta Q_d^0 = 2\pi/d$ and thickness $\Delta Q_h^0 = 2\pi/h$ oriented perpendicular to the incident beam direction. For a beam diameter of 0.5 µm and a path length through the SiGe SL structure of 2 µm the numerical values of these quantities are $\Delta Q_d^0 = 1.3 \times 10^{-3}$ Å^{-1} and $\Delta Q_h^0 = 0.3 \times 10^{-3}$ Å^{-1}. In addition, we have to take into account the beam focusing caused by the FZP. This gives rise to a resolution function which can also be considered as a disc, with a diameter defined by the beam divergence $\Delta\theta_0$ and a thickness by the detector pixel size $\Delta\theta_s$ (see Fig. 2*b*). Since for our experiment the beam divergence and the pixel size were 0.08 and 0.003°, respectively, the corresponding diameter and thickness of the resolution function disc are $\Delta Q_d = 7.8 \times 10^{-3}$ Å^{-1} and $\Delta Q_h = 0.26 \times 10^{-3}$ Å^{-1}, respectively (Falub *et al.*, 2013). Thus, in view of the large beam divergence, the diameter of the resolution function disc (ΔQ_d) is approximately six times larger than the diameter of the diffraction peak disc (ΔQ_d^0) resulting from the finite crystal size. However, since these two discs have similar thicknesses ($\Delta Q_h \simeq \Delta Q_h^0$), and the aspect ratio of the larger one is ∼20, the cross section along the Q_h direction (*i.e.* parallel to the incidence wavevector $\mathbf{K}_0$) is in practice determined by the pixel detector size, $\Delta Q_h \simeq 0.26 \times 10^{-3}$ Å^{-1}. Thus, the width of the diffraction peak along Q_h can be a good measure of the crystal quality.

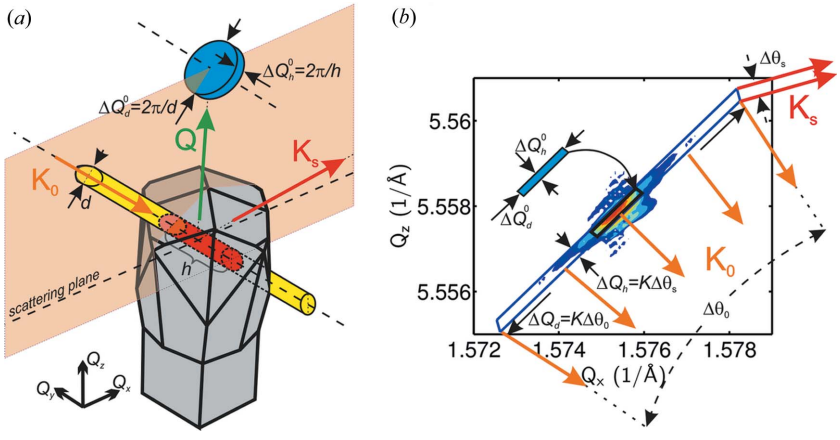

Figure 2
(*a*) Schematic sketch of a scanning X-ray nanodiffraction experiment on a facetted microcrystal. A nanofocused X-ray beam (yellow cylinder of diameter d) with the incidence wavevector $\mathbf{K}_0$ illuminates a top facet, crosses the crystal and exits through the sidewall. The scattered radiation from the irradiated crystal volume (red cylinder of length h) is represented by the wavevector $\mathbf{K}_s$. The diffraction peak in reciprocal space corresponding to the scattering vector $\mathbf{Q}$ is the Fourier transform of the irradiated crystal volume, depicted by the blue disc (diameter $\Delta Q_d^0 = 2\pi/d$ and thickness $\Delta Q_h^0 = 2\pi/h$) perpendicular to the incident beam. (*b*) Simulated three-dimensional RSM around the 115 reciprocal space point projected onto the Q_xQ_z plane for an SiGe microcrystal from Fig. 1(*a*), irradiated by a nanofocused X-ray beam. The shape of the diffraction peak is illustrated by the blue rectangle (length ΔQ_d^0 and width ΔQ_h^0) in the inset, which corresponds to the blue disc in panel (*a*). During a nanodiffraction experiment the scattered intensity is further smeared out by the convolution with the experimental resolution function (blue parallelogram) induced by the X-ray beam divergence $\Delta\theta_0$ and detector resolution (*i.e.* pixel size) $\Delta\theta_s$. In our case the additional peak broadening by the limited detector resolution is much less significant than that caused by beam divergence.

4. Results

Symmetric and asymmetric diffractions obtained with the laboratory source both show that the 8 µm tall SiGe crystals used as buffer between the Si substrate and the SiGe/Ge SL structures are completely strain relaxed and have a Ge content of ∼91.2%, close to the nominal 90%. The SL structure is represented in reciprocal space by a series of satellites having their zeroth-order maximum at a position coinciding with the relaxed SiGe crystal peak. This proves that the SL structure is lattice matched to the relaxed SiGe buffer.

Since the SL structure is grown on top of SiGe crystals which are terminated by {113} facets, the SL satellites are arranged along the crystal truncation rods corresponding to crystallographic ⟨113⟩ directions [see the dashed oblique lines in Figs. 3(*a*) and 3(*b*)]. The intensity scan obtained by slicing the 004 RSM along the [113] direction, combined with a simulation (Meduna *et al.*, 2007), provides the structural parameters of the SL structure (see Fig. 3*d*). The Ge content of the SiGe quantum barriers and the period of the SL structure are found to be 87 (1)% and 43.3 (2) nm, respectively. For the individual thicknesses of the Ge and SiGe layers we obtain 15.6 (5) and 27.5 (5) nm, respectively. The equivalent intensity scan obtained by slicing the 004 RSM along the [$\bar{1}\bar{1}3$] direction gives practically the same periodicity and layer thicknesses. The deviations of the layer thicknesses from the nominal ones can be attributed to the rather poor thickness uniformity offered by the LEPECVD reactor.

As mentioned above, the SL-containing SiGe crystals are terminated mainly by four equivalent {113} facets, namely (113), ($\bar{1}$13), (1$\bar{1}$3) and ($\bar{1}\bar{1}$3). A closer inspection of the measured RSMs reveals that the four equivalent {111} facets, namely (111), ($\bar{1}$11), (1$\bar{1}$1) and ($\bar{1}\bar{1}$1), are also present (Bergamaschini *et al.*,

2013). Each of these facets, of course, gives rise to a truncation rod perpendicular to its plane. The truncation rods observed in the asymmetric 224 RSM are depicted by dashed lines in Fig. 3(*b*). Taking into account that the scattering plane is perpendicular to the (001) sample surface and contains the [110] direction, we expect the presence of truncation rods along [111], [$\bar{1}\bar{1}1$], [113] and [$\bar{1}\bar{1}3$], which are indeed observed. Surprisingly, however, both the symmetric 004 RSM of Fig. 3(*a*) and the asymmetric 224 RSM of Fig. 3(*b*) contain reflections apparently belonging to a truncation rod along the vertical [001] direction, despite the lack of (001) facets on the crystals (see Fig. 1). In order to explain this peculiarity, we have to realize that the resolution out of the scattering plane in a typical high-resolution X-ray diffraction measurement with double-crystal monochromator and analyzer crystals is actually very low. In other words, the intensity is always integrated along the Q_y direction, such that the measured RSM is a projection of reciprocal space onto the Q_xQ_z plane.

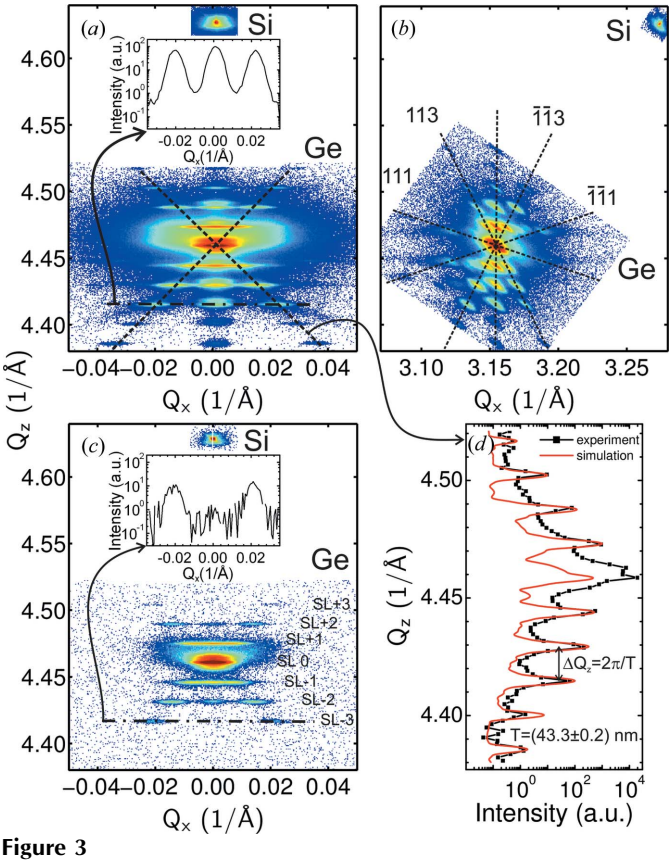

Figure 3
Reciprocal space maps using different beam collimations. (*a*) Symmetrical 004 and (*b*) asymmetrical 224 Q_xQ_z reciprocal space maps of a dense SiGe crystal array with the SL structure on top. Measurements were made with a rotating anode laboratory source and a highly collimated beam in the Q_xQ_z scattering plane, but totally noncollimated in the Q_y direction perpendicular to the scattering plane. The 004 RSM in panel (*c*) was collected with the same conditions as the RSM in panel (*a*) but using collimating Soller slit optics in the Q_y direction. Insets in panels (*a*) and (*c*) demonstrate the suppression of the central peak in the case of the collimated beam, proving its origin from the (1$\bar{1}$3) and ($\bar{1}$13) facets. The crosscut along the (113) truncation rod (*d*) shows the excellent agreement between experiment (black points) and simulations (red line), demonstrating the high periodicity of the SL structure.

As a result, the RSM may contain contributions from truncation rods for which $Q_y \neq 0$, for example, those along [1$\bar{1}$1], [$\bar{1}$11], [1$\bar{1}$3] and [$\bar{1}$13]. Projected along Q_y the latter two are expected to give rise to maxima at exactly the same Q_z as the truncation rods along [113] and [$\bar{1}\bar{1}$3], as is indeed observed in Figs. 3(*a*) and 3(*b*).

We were able to minimize $Q_y \neq 0$ contributions to the RSM around the symmetric 004 Bragg peak even in our laboratory setup by drastically reducing the angular aperture of the Soller slit blades parallel to the scattering plane. Thus, whereas the RSM of Fig. 3(*a*) was recorded with apertures of 2.5° in the incident beam and 5° in the exit beam, the RSM of Fig. 3(*c*) was obtained with corresponding apertures of 0.25° in the incident beam and only 0.115° in the exit beam. Therefore, in Fig. 3(*c*) the intensity is integrated over a narrow region in reciprocal space of width $\Delta Q_y \simeq 0.03$ Å^{-1}, whereas in Fig. 3(*a*) it is integrated over a larger region of width $\Delta Q_y \simeq 0.1$ Å^{-1}.

According to Fig. 3(*c*) the SL satellites of order > 2 on the streak along [001] completely disappear upon increasing the Q_y resolution, while the intensity of the second-order satellite at $Q_x = 0$ is significantly reduced with respect to that of satellites of the same order at $Q_x \neq 0$. A comparison of the cross sections along Q_x through the third-order peaks is shown in the insets of Figs. 3(*a*) and 3(*c*), corroborating the conclusion drawn from the visual inspection of the RSMs. This finally proves that the SL satellites on the vertical streak along the [001] direction originate from the (1$\bar{1}$3) and ($\bar{1}$13) facets. Deeper insight into the shape of SL peaks can be obtained by performing diffraction experiments with a synchrotron radiation beam collimated in both directions and using a two-dimensional detector.

The three-dimensional RSMs measured by the nanofocused synchrotron radiation beam were collected at various positions of an individual isolated SiGe crystal. The diffracted signal provides structural information on the SL structure, both in the trenches between SiGe crystals and on their top. Figs. 4(*a*) and 4(*b*) show Q_xQ_z and Q_yQ_z slices through the three-dimensional RSM obtained at the top of the crystal for $Q_y = 0.006$ Å^{-1} and $Q_x = 1.572$ Å^{-1}, with respective widths of $\Delta Q_y = \Delta Q_x = 0.001$ Å^{-1}. In Fig. 4(*c*) the projection along Q_z rather than a Q_yQ_x slice is shown, since the SL peaks along ⟨113⟩ truncation rods do not lie in the Q_yQ_x plane corresponding to the (001) sample surface. The colored arrows pointing at the SEM micrographs in the insets to the RSMs illustrate the geometry of the irradiating X-ray beam. Since the incident beam impinges on the central top part of the crystal, all four equivalent {113} facets contribute to the signal. From the two reciprocal space sections of Figs. 4(*a*) and 4(*b*) and the projection of Fig. 4(*c*) we clearly see that the distributions of the SL satellites from the top surface facets are aligned along the four truncation rods, forming a tetrapod (see also Fig. 5*a*). The diffuse broad intensity present as background around the sharp SL peaks and around the apparent (001) truncation rod in between originate from the SiGe material in trenches.

As mentioned in §3, in view of the beam divergence induced by the FZP, the shape of the resolution function has the form

of an oblique narrow disc. Such discs were also observed at the positions of the SL satellite peaks, which are schematically represented in Figs. 4(*d*)–4(*f*). Thus, for the RSM section in the Q_xQ_z plane the SL peaks are shaped as oblique rectangles (see Figs. 4*a* and 4*d*). For the RSM section in the Q_yQ_z plane the peaks appear as horizontal rectangles (see Figs. 4*b* and 4*e*), and finally in the projection onto the Q_yQ_x plane the peaks are seen as circles (see Figs. 4*c* and 4*f*). If instead of the narrow slice of width ΔQ_x in Fig. 4(*b*) we had used the projection onto the Q_yQ_z plane, the SL peaks would have appeared as circles as well [see the dashed circles in Fig. 4(*e*)]. Figs. 4(*e*) and 4(*f*) explain the effect of the Soller slit blades used in the laboratory experiment described above, where the second- and higher-order maxima for $Q_y = 0$ are drastically suppressed. The light-yellow region II indicates the satellites stemming from the $[1\bar{1}3]$ and $[\bar{1}13]$ rods, which would be visible in the laboratory experiment for the small-aperture Soller slits limiting Q_y to below 0.03 Å^{-1}, as depicted in Fig. 3(*c*). The aperture of the Soller slits used to record the RSM in Fig. 3(*a*) is ∼2 times larger than the Q_y range in Fig. 4(*c*).

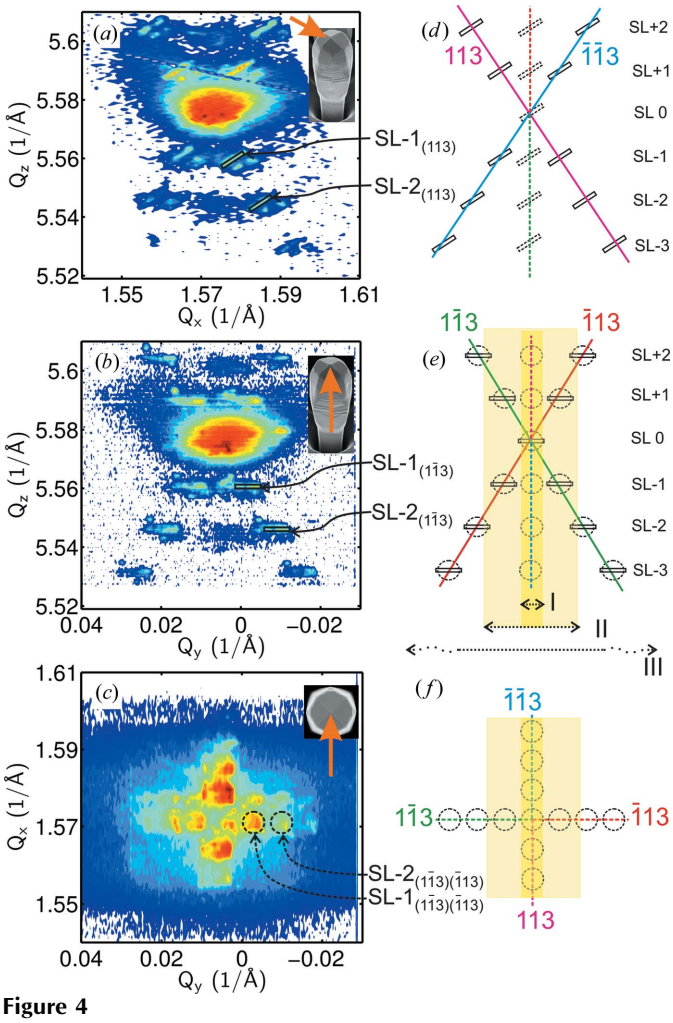

Figure 4
Probing the SL crystal structure with a nanofocused synchrotron radiation beam. Slices through the three-dimensional RSM of width $\Delta Q = 0.001$ Å^{-1} for (*a*) $Q_y = 0.006$ Å^{-1} and (*b*) $Q_x = 1.572$ Å^{-1}, and (*c*) projection onto the Q_xQ_y plane integrated along Q_z, recorded at the top center of the Ge crystal. The inset SEM micrograph shows schematically the position of the X-ray beam with respect to the cross section/projection plane. The schematics in (*d*), (*e*) and (*f*) show the distribution of SL peaks along significant crystallographic directions corresponding to the top crystal facets, *i.e.* (113), (1$\bar{1}$3), ($\bar{1}$13) and ($\bar{1}\bar{1}$3). The solid lines correspond to the peak shapes and truncation rods observed in the corresponding cross section through the three-dimensional RSM, and the dashed lines indicate these as they would be observed out of the realized cross section, *e.g.* when projected onto the corresponding plane. In the case of a nanofocused synchrotron beam, the SL peaks are observed as oblique narrow discs owing to the large divergence of the X-ray beam induced by the Fresnel focusing system (see Falub *et al.*, 2013). In panels (*e*) and (*f*) the yellow area demonstrates the Q_xQ_z slice where the intensity is integrated over Q_y. I – focused synchrotron beam, as plotted in panel (*a*). II – beam collimated by Soller optics, as plotted in Fig. 3(*b*). III – beam with high divergence in Q_y, as from a laboratory X-ray tube.

The projection of the three-dimensional RSM onto the Q_yQ_x plane in Fig. 4(*c*) clearly shows that the SL peaks exhibit fourfold symmetry and are distributed along the four ⟨113⟩ truncation rods. In order to observe the satellite peaks, the central part of the signal around the zeroth-order reflection was suppressed and the intensity thus summed along the Q_z axis without the large signal from the pure SiGe buffer crystal. Examples of two (SL-1 and SL-2) satellites are depicted in Figs. 4(*a*)–4(*c*). Finally, we show in Fig. 5(*a*) the full three-dimensional RSM in the form of a conveniently chosen iso-level surface of the scattering intensity. This RSM was obtained from the apex of the SiGe crystal. The SL peaks are therefore visible on all four truncation rods in Fig. 5(*a*). In order to improve the visibility of the SL peaks, the iso-level surface was plotted after removing the signal stemming from defective material in the trenches, which is superimposed on the zeroth-order SL peak. To highlight the fourfold symmetry of this three-dimensional RSM we have connected the SL peaks of equal order lying in the colored horizontal planes by white dashed lines.

Now that we have discussed the three-dimensional diffraction pattern obtained with a nanofocused X-ray beam, we are in a position to make full use of the power of scanning nanodiffraction. According to Figs. 5(*b*)–5(*g*) and Figs. 6(*b*)–6(*e*) the size of the top four crystal facets is in the range of 2–2.5 µm. Since the nanofocused beam is about six times smaller, we expect to obtain local structural information within each facet of the SL crystal. From the three-dimensional RSM we can select a range of interest in reciprocal space and map the scattering intensity in the real-space *xy* plane. To illustrate this, we select the area around the SL-1 peak, lying on a truncation rod belonging to one of the {113} facets. The X-ray beam is then scanned across the chosen facet and the scattering intensity is recorded at the nodes of a conveniently chosen *xy* surface mesh of step size $\Delta x = \Delta y = 500$ nm. Figs. 5(*b*)–5(*e*) show the resulting intensity distributions obtained by carrying out this procedure for all four equivalent {113} facets. Evidently, the four different facets can easily be recognized from these figures. The facet structure becomes even more apparent by superimposing the intensity distributions obtained from all four equivalent {113} truncation rods as depicted in Fig. 5(*f*). The shape of the reconstructed intensity obtained by scanning nanodiffraction at an incidence angle of 47.4° perfectly coincides with the surface morphology of the SL crystal, as shown by the superimposed SEM micrograph in

Fig. 5(*g*). Surprisingly, even the small edges between {113} and {111} facets are closely reproduced. In order to compare the intensity mesh with the perspective-view SEM micrograph (tilt angle of 45°), the panels in Fig. 5 are all oriented as seen from (or close to) the direction of the incident beam. On the other hand, Fig. 1 is a side view of the scattering plane to illustrate the experimental geometry.

Of course, our measurement provides not only the facet morphology but also the structural parameters of the SL, such as the period and the layer thicknesses, on a local scale. As an illustration, let us select a point in the middle of each of the four {113} facets. At each point we make a cross section through the disc-shaped SL-1 peak in the RSM along the Q_h axis, parallel to the $\mathbf{K}_0$ direction. In Fig. 6(*a*) the cross sections obtained for all four facets reveal that the SL peaks are as narrow as the Si substrate peak ($\Delta Q_h \simeq 0.5 \times 10^{-3}$ Å^{-1}), *i.e.* nearly as narrow as the theoretical diffraction peak corresponding to the finite size of the irradiated volume ($\Delta Q_h^0 \simeq 0.3 \times 10^{-3}$ Å^{-1}). It is important to point out here that these widths are measured along Q_h, where, as pointed out below, the beam divergence plays a minor role. The peak widths measured in this direction are therefore indeed a good indication of the high crystalline quality of both the SL structure and the SiGe crystal buffer underneath (Falub *et al.*, 2013). Please note also that the theoretical broadening of the diffraction peak for an ideal SL structure along the Q_z axis corresponding to the vertical growth direction is $\Delta Q_z \simeq 0.29 \times 10^{-3}$ Å^{-1}. We have previously shown by defect etching along with etch pit counting that faceted crystals of the kind considered here are indeed defect free (Falub *et al.*, 2012; Marzegalli *et al.*, 2013). The peak broadening along Q_x in Fig. 3, measured with the broad beam laboratory setup, is thus due to random tilts of the crystals, hundreds of thousands of which are measured at once.

Moreover, cross sections taken along various truncation rods reveal the complete SL diffraction pattern at chosen positions on the crystal surface. Applying again the power of scanning nanodiffraction, we can also map the SL period over the whole crystal surface as shown in Figs. 6(*b*)–6(*e*). The precision at which the structural parameters of the SL can be obtained is, however, limited because of the distorted shape of the experimental peaks arising from the inhomogeneity of the resolution function of the FZP mentioned before. Additionally, the measured SL peaks broaden when the beam hits the facet at an oblique angle. We recall that the SL peaks are not perfect discs, as indicated for example in the area inside the circles in Fig. 4(*c*). By averaging over the disc size given by the beam divergence (Falub *et al.*, 2013) we have nevertheless

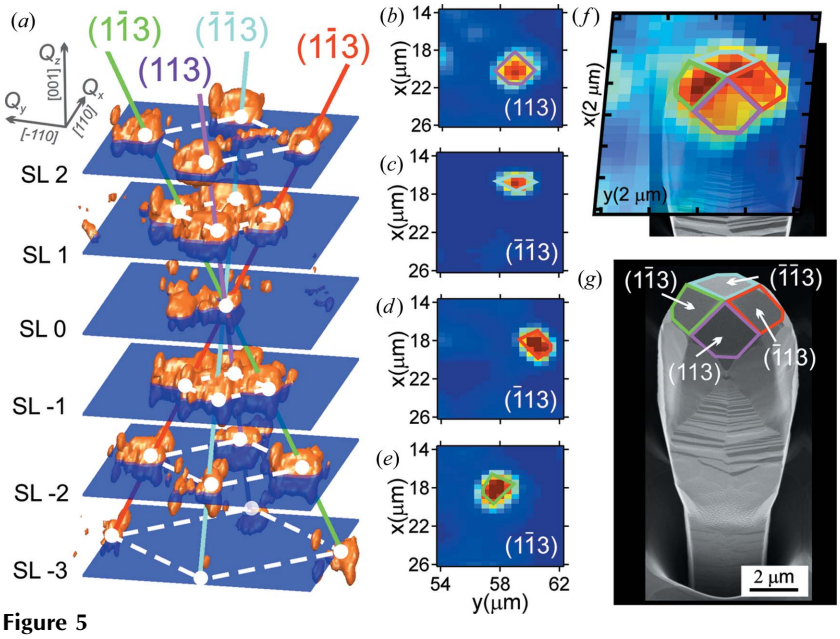

Figure 5
Reconstruction of the SL crystal top morphology. (*a*) Three-dimensional RSM around the 115 reciprocal space point as an iso-level surface plot recorded in the middle of the crystal where all four truncation rods corresponding to the four equivalent {113} top facets are observed. To enhance the fourfold symmetry of the SL peak positions, horizontal planes for individual SL orders were drawn, and the SL peaks of one order are connected by white dashed lines. (*b*), (*c*), (*d*), (*e*) The mesh of the signal from SL peaks for the individual truncation rods over an *xy* surface indicates the position of particular surface facets. (*f*) By summing the intensity maps over the surface for all SL-1 peaks, the SL crystal shape is reconstructed in one surface map recorded around the incidence angle of 47.4°. It perfectly matches the perspective-view SEM micrograph (tilt angle of 45°) (*g*) of a 8 μm tall Ge crystal with crystallographic facets (113), ($\bar{1}$13), ($\bar{1}$13) and (1$\bar{1}$3).

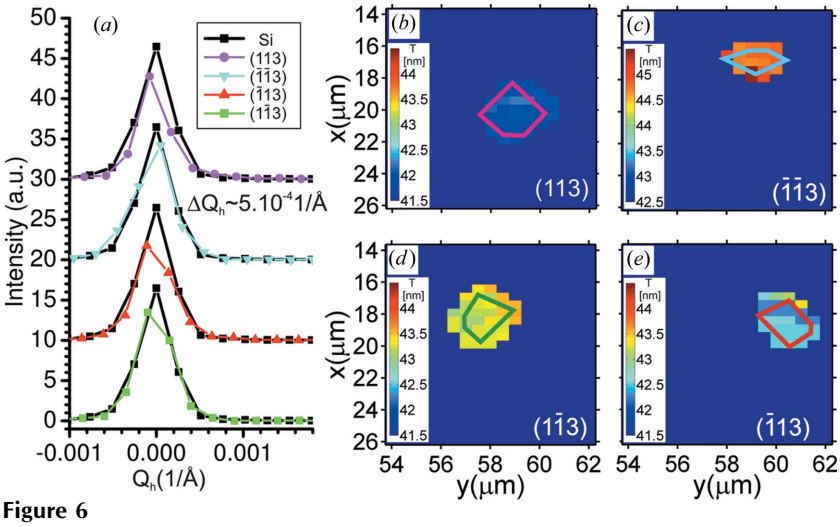

Figure 6
Peak widths and SL period mapping on different crystal facets. (*a*) Cross sections along the direction Q_h through the SL-1 diffraction peaks for truncation rods of all facets compared with the width of the Si substrate peak. Maps of SL periodicity obtained along particular truncation rods corresponding to individual facets: (*b*) facet (113); (*c*) facet ($\bar{1}$13); (*d*) facet ($\bar{1}$13); (*e*) facet (1$\bar{1}$3).

been able to obtain the SL periods mapped over individual facets with a precision better than 5%.

Maps of the SL periodicity corresponding to the intensity maps of Figs. 5(*b*)–5(*e*) can be seen in Figs. 6(*b*)–6(*e*). We found that the layer periodicity does not vary within the experimental error of about 1 nm across each individual facet. Small variations of the periodicity were, however, detected between different facets. In particular, we obtained local SL periods of 42.0 (6), 44.6 (15), 43.4 (8) and 42.8 (8) nm for the (113), ($\overline{1}$13), ($\bar{1}$13) and (1$\bar{1}$3) facets, respectively. Apparently, the error in the SL period is highest for the ($\overline{1}$13) facet, since the beam impinges on this facet at the most oblique incidence angle. The smallest error of the SL period was obtained for the (113) facet, for which the incident beam is almost perpendicular. The periodicity averaged over all four {113} facets is in good agreement with the laboratory data, the signal of which stems from averaging over thousands of SL crystals. Unfortunately, the thickness ratio for the SiGe/Ge bilayer could not be obtained from the nanodiffraction experiments owing to the large uncertainty induced by the inhomogeneity of the resolution function and the resulting distortion of the SL peaks.

5. Conclusion

In conclusion, we have used scanning X-ray nanodiffraction to probe both the facet morphology and the crystal quality of three-dimensional micrometre-sized epitaxial SiGe crystals grown on patterned Si substrates. The presence of periodic SiGe/Ge heterostructures on top of the SiGe crystals permitted the accurate reconstruction of the crystal shapes without the need of any structural model. While the structural parameters revealed the high crystal quality of the SL stacks themselves, the present accuracy is not yet sufficient to determine variations of SL properties at the nanoscale. By combining this straightforward model-free method with much sharper synchrotron X-ray beams (*e.g.* below 5 nm), non-destructive imaging of structural properties and crystal morphology at unprecedented resolution is expected to become possible soon. The advantage of the method becomes evident, for example, when mapping the shape of small crystals buried inside materials transparent to X-rays (*e.g.* photoresist layers), which otherwise would be inaccessible to other microscope probes.

This work was supported by the Swiss federal funding program Nano-Tera through project NEXRAY. One author wishes to acknowledge the projects INGO LG 13058, Research4Industry (CZ.1.07/2.4.00/17.0006), NANOE – EE2.3.20.0027 and ED1.1.00/02.0068. We acknowledge the staff of the ID01 beamline at the European Synchrotron Radiation Facility, Grenoble; Centre Suisse d'Electronique et Microtechnique for supplying the patterned Si substrates; FIRST Center for Micro- and Nanoscience of ETH Zürich; EMEZ electron microscopy ETH Zürich; and helpful discussions with B. Batlogg and A. Dommann.

References

Bartosik, M., Daniel, R., Mitterer, C., Matko, I., Burghammer, M., Mayrhofer, P. & Keckes, J. (2013). *Thin Solid Films*, **542**, 1–4.
Bergamaschini, R., Isa, F., Falub, C. V., Niedermann, P., Müller, E., Isella, G., von Känel, H. & Miglio, L. (2013). *Surf. Sci. Rep.* **68**, 390–417.
Biermanns, A., Carbone, D., Breuer, S., Jacques, V. L. R., Schulli, T., Geelhaar, L. & Pietsch, U. (2013). *Phys. Status Solidi RRL*, **7**, 860–863.
Chamard, V., Stangl, J., Carbone, G., Diaz, A., Chen, G., Alfonso, C., Mocuta, C. & Metzger, T. H. (2010). *Phys. Rev. Lett.* **104**, 165501.
Chrastina, D., Vanacore, G. M., Bollani, M., Boye, P., Schöder, S., Burghammer, M., Sordan, R., Isella, G., Zani, M. & Tagliaferri, A. (2012). *Nanotechnology*, **23**, 155702.
Cornelius, T. W., Carbone, D., Jacques, V. L. R., Schülli, T. U. & Metzger, T. H. (2011). *J. Synchrotron Rad.* **18**, 413–417.
Davies, R. J., Burghammer, M. & Riekel, C. (2009). *J. Synchrotron Rad.* **16**, 22–29.
Döring, F., Robisch, A., Eberl, C., Osterhoff, M., Ruhlandt, A., Liese, T., Schlenkrich, F., Hoffmann, S., Bartels, M., Salditt, T. & Krebs, H. (2013). *Opt. Express*, **21**, 19311–19323.
Dubslaff, M., Hanke, M., Patommel, J., Hoppe, R., Schroer, G. C., Schöder, S. & Burghammer, M. (2012). *Nanoscale Res. Lett.* **7**, 553.
Dubslaff, M., Hanke, M., Schöder, S., Burghammer, M., Boeck, T. & Patommel, J. (2010). *Appl. Phys. Lett.* **96**, 133107.
Falub, C. V., von Känel, H., Isa, F., Bergamaschini, R., Marzegalli, A., Chrastina, D., Isella, G., Müller, E., Niedermann, P. & Miglio, L. (2012). *Science*, **335**, 1330–1334.
Falub, C. V., Kreiliger, T. *et al.* (2014). *Thin Solid Films*, **557**, 42–49.
Falub, C. V., Meduňa, M., Chrastina, D., Isa, F., Marzegalli, A., Kreiliger, T., Taboada, A. G., Isella, G., Miglio, L., Dommann, A. & von Känel, H. (2013). *Sci. Rep.* **3**, 2276.
Godard, P., Carbone, G., Allain, M., Mastropietro, F., Chen, G., Capello, L., Diaz, A., Metzger, T. H., Stangl, J. & Chamard, V. (2011). *Nat. Commun.* **1569**, 1–6.
Hanke, M., Dubslaff, M., Schmidbauer, M., Boeck, T., Schöder, S., Burghammer, M., Riekel, C., Patommel, J. & Schroer, C. G. (2008). *Appl. Phys. Lett.* **92**, 193109.
Hrauda, N., Zhang, J., Wintersberger, E., Etzelstorfer, T., Mandl, B., Stangl, J., Carbone, D., Holý, V., Jovanović, V., Biasotto, C., Nanver, L. K., Moers, J., Grützmacher, D. & Bauer, G. (2011). *Nano Lett.* **11**, 2875–2880.
Hruszkewycz, S. O., Holt, M. V., Murray, C. E., Bruley, J., Holt, J., Tripathi, A., Shpyrko, O. G., McNulty, I., Highland, M. J. & Fuoss, P. H. (2012). *Nano Lett.* **12**, 5148–5154.
Krüger, S. P., Neubauer, H., Bartels, M., Kalbfleisch, S., Giewekemeyer, K., Wilbrandt, P. J., Sprung, M. & Salditt, T. (2012). *J. Synchrotron Rad.* **19**, 227–236.
Marzegalli, A., Isa, F., Groiss, H., Müller, E., Falub, C. V., Taboada, A. G., Niedermann, P., Isella, G., Schäffler, F., Montalenti, F., von Känel, H. & Miglio, L. (2013). *Adv. Mater.* **25**, 4408–4412.
Meduňa, M., Novák, J., Bauer, G., Holý, V., Falub, C. V., Tsujino, S. & Grützmacher, D. (2007). *Semicond. Sci. Technol.* **22**, 447–453.
Mimura, H., Handa, S., Kimura, T., Yumoto, H., Yamakawa, D., Yokoyama, H., Matsuyama, S., Inagaki, K., Yamamura, K., Sano, Y., Tamasaku, K., Nishino, Y., Yabashi, M., Ishikawa, T. & Yamauchi, K. (2010). *Nat. Phys.* **6**, 122–125.
Mocuta, C., Stangl, J., Mundboth, K., Metzger, T. H., Bauer, G., Vartanyants, I. A., Schmidbauer, M. & Boeck, T. (2008). *Phys. Rev. B*, **77**, 245425.
Mondiali, V., Bollani, M., Cecchi, S., Richard, M. I., Schülli, T., Chahine, G. & Chrastina, D. (2014). *Appl. Phys. Lett.* **104**, 021918.
Paci, B., Bailo, D., Albertini, V. R., Wright, J., Ferrero, C., Spyropoulos, G. D., Stratakis, E. & Kymakis, E. (2013). *Adv. Mater.* **25**, 4760–4765.
Pezzoli, F., Isa, F., Isella, G., Falub, C. V., Kreiliger, T., Salvalaglio, M., Bergamaschini, R., Grilli, E., Guzzi, M., von Känel, H. & Miglio, L. (2014). *Phys. Rev. Appl.* **1**, 044005.

Pfeifer, M. A., Williams, G. J., Vartanyants, I. A., Harder, R. & Robinson, I. K. (2006). *Nature*, **442**, 63–66.
Pietsch, U., Holý, V. & Baumbach, T. (2004). *High Resolution X-ray Scattering: From Thin Films to Lateral Nanostructures*. Berlin: Springer.
Robinson, I. & Harder, R. (2009). *Nat. Mater.* **8**, 291–298.
Rosenblad, C., von Känel, H., Kummer, M., Dommann, A. & Müller, E. (2000). *Appl. Phys. Lett.* **76**, 427–429.
Scheler, T., Rodrigues, M., Cornelius, T. W., Mocuta, C., Malachias, A., Magalhães-Paniago, R., Comin, F., Chevrier, J. & Metzger, T. H. (2009). *Appl. Phys. Lett.* **94**, 023109.
Stangl, J., Mocuta, C., Chamard, V. & Carbone, D. (2014). *Nanobeam X-ray Scattering: Probing Matter at the Nanoscale.* Weinheim: Willey-VCH.
Stangl, J., Mocuta, C., Diaz, A., Metzger, T. H. & Bauer, G. (2009). *Chem. Phys. Chem.* **10**, 2923–2930.
Stefenelli, M., Todt, J., Riedl, A., Ecker, W., Müller, T., Daniel, R., Burghammer, M. & Keckes, J. (2013). *J. Appl. Cryst.* **46**, 1378–1385.
Takahashi, Y., Zettsu, N., Nishino, Y., Tsutsumi, R., Matsubara, E., Ishikawa, T. & Yamauchi, K. (2010). *Nano Lett.* **10**, 1922–1926.